nature materials

ARTICLES

https://doi.org/10.1038/s41563-019-0369-5

Anisotropic spin fluctuations in detwinned FeSe

Tong Chen[1], Youzhe Chen[2], Andreas Kreisel[3], Xingye Lu[4*], Astrid Schneidewind[5], Yiming Qiu[6], J. T. Park[7], Toby G. Perring[8], J Ross Stewart[8], Huibo Cao[9], Rui Zhang[1], Yu Li[1], Yan Rong[4], Yuan Wei[10], Brian M. Andersen[11], P. J. Hirschfeld[12], Collin Broholm[2,6] and Pengcheng Dai[1,4*]

Superconductivity in FeSe emerges from a nematic phase that breaks four-fold rotational symmetry in the iron plane. This phase may arise from orbital ordering, spin fluctuations or hidden magnetic quadrupolar order. Here we use inelastic neutron scattering on a mosaic of single crystals of FeSe, detwinned by mounting on a $BaFe_2As_2$ substrate to demonstrate that spin excitations are most intense at the antiferromagnetic wave vectors $\mathbf{Q}_{AF}=(\pm1, 0)$ at low energies $E=6$–11 meV in the normal state. This two-fold (C_2) anisotropy is reduced at lower energies, 3–5 meV, indicating a gapped four-fold (C_4) mode. In the superconducting state, however, the strong nematic anisotropy is again reflected in the spin resonance ($E=3.6$ meV) at $\mathbf{Q}_{AF}$ with incommensurate scattering around 5–6 meV. Our results highlight the extreme electronic anisotropy of the nematic phase of FeSe and are consistent with a highly anisotropic superconducting gap driven by spin fluctuations.

High-transition-temperature superconductivity in copper- and iron-based materials emerges from their antiferromagnetic (AF) ordered non-superconducting parent compounds[1]. While the parents of copper oxide superconductors are Mott insulators with a simple chequerboard AF structure[1], most iron pnictide parent materials exhibit a tetragonal-to-orthorhombic structural transition at T_s (<295 K) and form twin domains before ordering antiferromagnetically at T_N ($T_s \geq T_N$) (ref. [2]). Therefore, we must detwin iron pnictides to measure their intrinsic electronic properties below T_s. By applying a uniaxial pressure along one axis of the orthorhombic lattice to detwin the sample, an in-plane resistivity anisotropy has been observed in strained iron pnictides $BaFe_{2-x}T_xAs_2$ (where T is Co or Ni) above T_s (refs. [3,4]). The resistivity anisotropy has been ascribed to an electronic nematic phase that spontaneously breaks the rotational symmetry while preserving the translation symmetry of the underlying lattice, and is established in the temperature regime below T_s and above T_N (refs. [5,6]). Below T_N, the AF structure is collinear, consisting of columns of antiparallel spins along the orthorhombic a_o axis and parallel spins along the b_o axis with an in-plane AF ordering wave vector $\mathbf{Q}_{AF}=(\pm1, 0)$ in reciprocal space[2].

The highly unusual iron-based superconductor FeSe exhibits an orthorhombic structural distortion and superconductivity without static AF order (Fig. 1a)[7–9]. Although the nematic phase in FeSe is established below T_s (≈90 K)[8], it has been argued that its nematic order and superconductivity are induced by orbital fluctuations (Fig. 1b)[10–14], forming a sign-preserving s^{++}-wave electron pairing, and therefore it would be fundamentally different from other iron-based superconductors[15]. Alternatively, the absence of static AF order in FeSe has been interpreted as evidence for a quantum paramagnet arising from the d-orbital spin-1 localized iron moments[16,17]. Here, the nematic phase is driven by magnetic frustration due to competition between low-energy spin fluctuations associated with AF collinear order and those associated with various types of staggered order[18]. Third, the nematic superconductivity in FeSe without AF order may arise from a frustration-induced nematic quantum spin liquid state with melted AF order[19]. This model predicts a dramatic suppression of the magnetic spectral weight at $\mathbf{Q}=(0, \pm1)$ in a detwinned sample, and explains the observed superconducting gap anisotropy by angle-resolved photoemission spectroscopy[20–22] and scanning tunnelling microscopy (STM)[23–25] experiments by an orbital-dependent Hund coupling[19]. Fourth, the nematic order may arise from a hidden magnetic quadrupolar order[26,27]. Finally, the nematic phase and superconductivity in FeSe have also been described in terms of itinerant electrons interacting among quasi-nested hole–electron Fermi surfaces[28,29], as in other iron-based superconductors[30]. In this picture, the electronic correlation effect is taken into account using orbital-dependent quasiparticle weights[24,31]. Without electron correlation effects, spin fluctuations in the nematic phase below T_s exhibit only a minor C_4 asymmetry. Including correlations in the theoretical calculations renders the spin fluctuations highly C_2 symmetric with negligible weight at $(0, \pm1)$, and a neutron spin resonance exhibited only at $\mathbf{Q}_{AF}=(\pm1, 0)$ driven by the d_{yz} orbitals[31]. Approaches based on localized models with magnetic quadrupolar order have also predicted a strong suppression of low-energy $(0, \pm1)$ intensity[27].

In recent inelastic neutron scattering (INS) experiments on twinned FeSe[18,32,33], well-defined low-energy ($E<15$ meV) spin fluctuations are found at $\mathbf{Q}_{AF}=(\pm1, 0)$ and its twin-domain positions $(0, \pm1)$ in the nematic phase below T_s. On cooling below the superconducting transition temperature T_c, ≈ 8 K, a neutron spin resonance, a key signature of unconventional superconductivity[1], appears at $E\approx4$ meV and sharply peaks at the $(\pm1, 0)$ and $(0, \pm1)$ positions[32,33]. Figure 1c shows the energy dependence of the magnetic scattering $S(E)$ integrated around $\mathbf{Q}_{AF}$ obtained from our high-resolution INS experiments (Methods). In the normal state,

[1]Department of Physics and Astronomy, Rice University, Houston, TX, USA. [2]Department of Physics and Astronomy, Johns Hopkins University, Baltimore, MD, USA. [3]Institut für Theoretische Physik, Universität Leipzig, Leipzig, Germany. [4]Center for Advanced Quantum Studies and Department of Physics, Beijing Normal University, Beijing, China. [5]Forschungszentrum Jülich GmbH, Jülich Center for Neutron Sciences at MLZ, Garching, Germany. [6]NIST Center for Neutron Research, National Institute of Standards and Technology, Gaithersburg, MD, USA. [7]Heinz Maier-Leibnitz Zentrum (MLZ), Technische Universität München, Garching, Germany. [8]ISIS Facility, STFC Rutherford-Appleton Laboratory, Didcot, UK. [9]Neutron Scattering Division, Oak Ridge National Laboratory, Oak Ridge, TN, USA. [10]Institute of Physics, Chinese Academy of Sciences, Beijing, China. [11]Niels Bohr Institute, University of Copenhagen, Copenhagen, Denmark. [12]Department of Physics, University of Florida, Gainesville, FL, USA. *e-mail: luxy@bnu.edu.cn; pdai@rice.edu

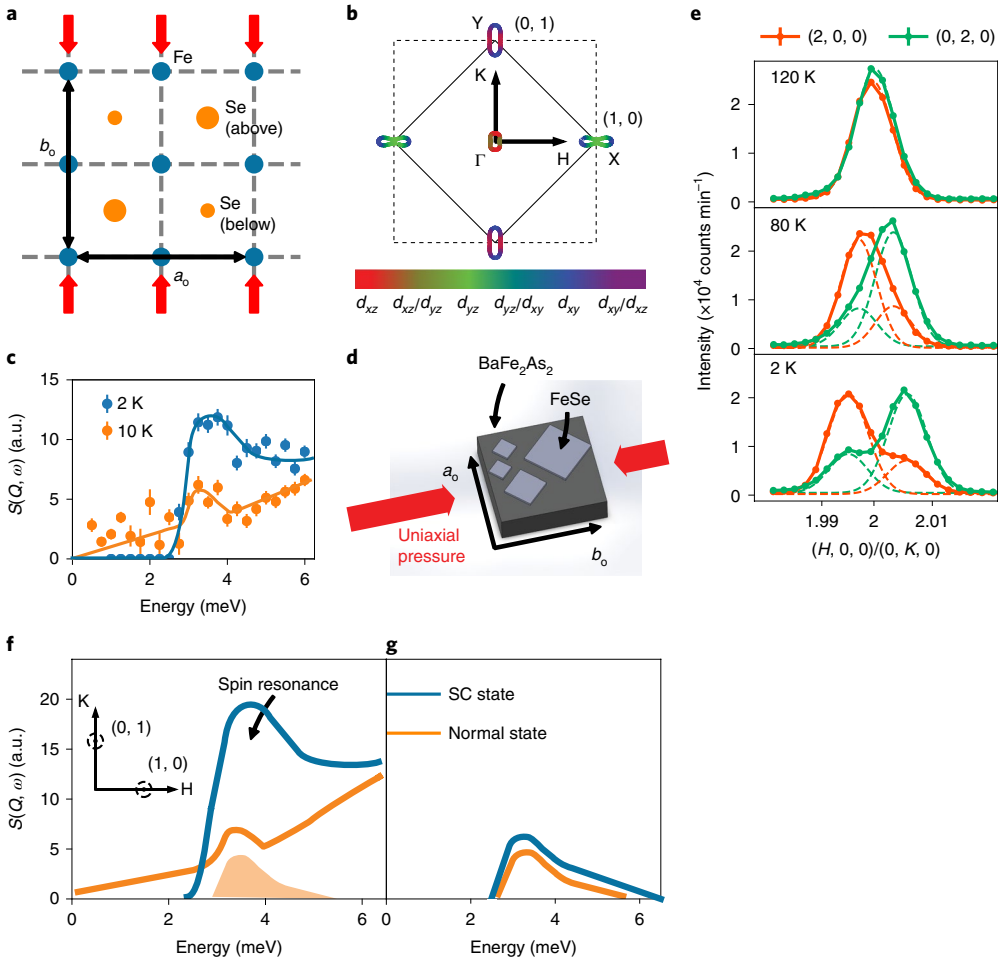

Fig. 1 | Crystal structure, Fermi surface and neutron scattering of FeSe. a, Crystal structure of FeSe, where blue and orange colours mark Fe and Se positions, respectively. The red arrows indicate the uniaxial strain direction applied through detwinned $BaFe_2As_2$. a_o and b_o are the orthorhombic lattice parameters (double-headed black arrows) in the nematic phase. Grey dashed lines are guides for the eye. **b**, Hole–electron Fermi surfaces of the tight-binding model for FeSe (ref. [24]). The colour indicates the orbital character of the Fermi surfaces, where red, green and blue indicate d_{xz}, d_{yz} and d_{xy} orbitals of the Fe atom. Fermi surface nesting of $\Gamma \rightarrow X$ and $\Gamma \rightarrow Y$ corresponds to (1, 0) and (0, 1) in reciprocal lattice units, where $(H, K) = (q_x a_o/2\pi, q_y b_o/2\pi)$ are in-plane Miller indices of the orthorhombic lattice, respectively (Methods). **c**, $S(\mathbf{Q}, E)$ integrated around (1, 0) above ($T = 10$ K) and below ($T = 2$ K) T_c (≈8 K) on twinned FeSe (Supplementary Fig. 5). The vertical error bars indicate the statistical errors of 1 s.d. **d**, Schematic diagram of the sample arrangement. FeSe samples are glued on large single crystals of $BaFe_2As_2$ under a uniaxial pressure of about 20 MPa (refs. [39,40]). **e**, Wave-vector scans of nuclear (2, 0, 0) and (0, 2, 0) Bragg peaks of FeSe on an assembly of $BaFe_2As_2$ single crystals at different temperatures. The dashed lines indicate the single-Gaussian components of the fitting. **f**,**g**, Schematic illustrations of the magnetic scattering at (1, 0) (**f**) and (0, 1) (**g**) in the normal and superconducting (SC) states estimated from the twinned and detwinned samples (Supplementary Fig. 10). The shaded region in **f** is (0, 1) data from **g**.

the magnetic scattering is gapless above $E = 0.5$ meV and increases in intensity with increasing energy (Fig. 2a). In addition to having a weak peak around $E \approx 3.2$ meV, we find that the scattering changes from well-defined commensurate peaks centred around $\mathbf{Q}_{AF}$ below $E = 3.625 \pm 0.125$ meV (Fig. 2b, c) to a peak with a flattish top at $E = 5.625 \pm 0.125$ meV (Fig. 2d). On cooling to below T_c in the superconducting state, the spin excitation spectra open a gap below $E \approx 2.5$ meV (Fig. 2e,f), form a commensurate resonance at $E = 3.6$ meV (Fig. 2g) and exhibit ring-like incommensurate scattering at $E = 5.25 \pm 0.075$ meV (Fig. 2f). The dispersive ring-like incommensurate resonance is also seen in hole-doped $Ba_{0.67}K_{0.33}(Fe_{1-x}Co_x)_2As_2$ superconductors[34].

Although these results on twinned FeSe suggest that spin fluctuations play an important role in the superconductivity of FeSe, they provide no information on the possible orbital-selective nature of the fluctuations, which may lead to a highly anisotropic electron pairing state[19,31,35–38]. From STM quasiparticle interference measurements on single-domain (detwinned) FeSe, where the Fermi surface geometry of electronic bands can be determined in the nematic phase, sign-reversed superconducting gaps are found at the hole (Γ or $\mathbf{Q} = (0, 0)$) and electron (X or $\mathbf{Q}_{AF} = (1, 0)$) Fermi surface states derived from d_{yz} orbitals of the Fe atoms along the orthorhombic a_o-axis direction (Fig. 1a,b)[24]. Moreover, similar STM measurements show that the same orbital-selective self-energy effects are already present in the normal state of FeSe above T_c (ref. [25]).

If superconductivity in FeSe arises from quasiparticle excitations between hole and electron pockets (Fig. 1b) that are indeed orbital selective[24,25], detwinned crystals should exhibit a strong anisotropy of the low-energy spin excitations. In particular, it is expected that the neutron spin resonance associated with $s^{\pm}$ superconductivity[32,33] should only occur along the orthorhombic a_o-axis direction at $\mathbf{Q}_{AF} = (\pm 1, 0)$ in detwinned FeSe, as the orbital-selective superconducting gap with the d_{yz} orbital character is large for scattering vectors along the a_o axis[24]. Similarly, orbital-dependent Hund's

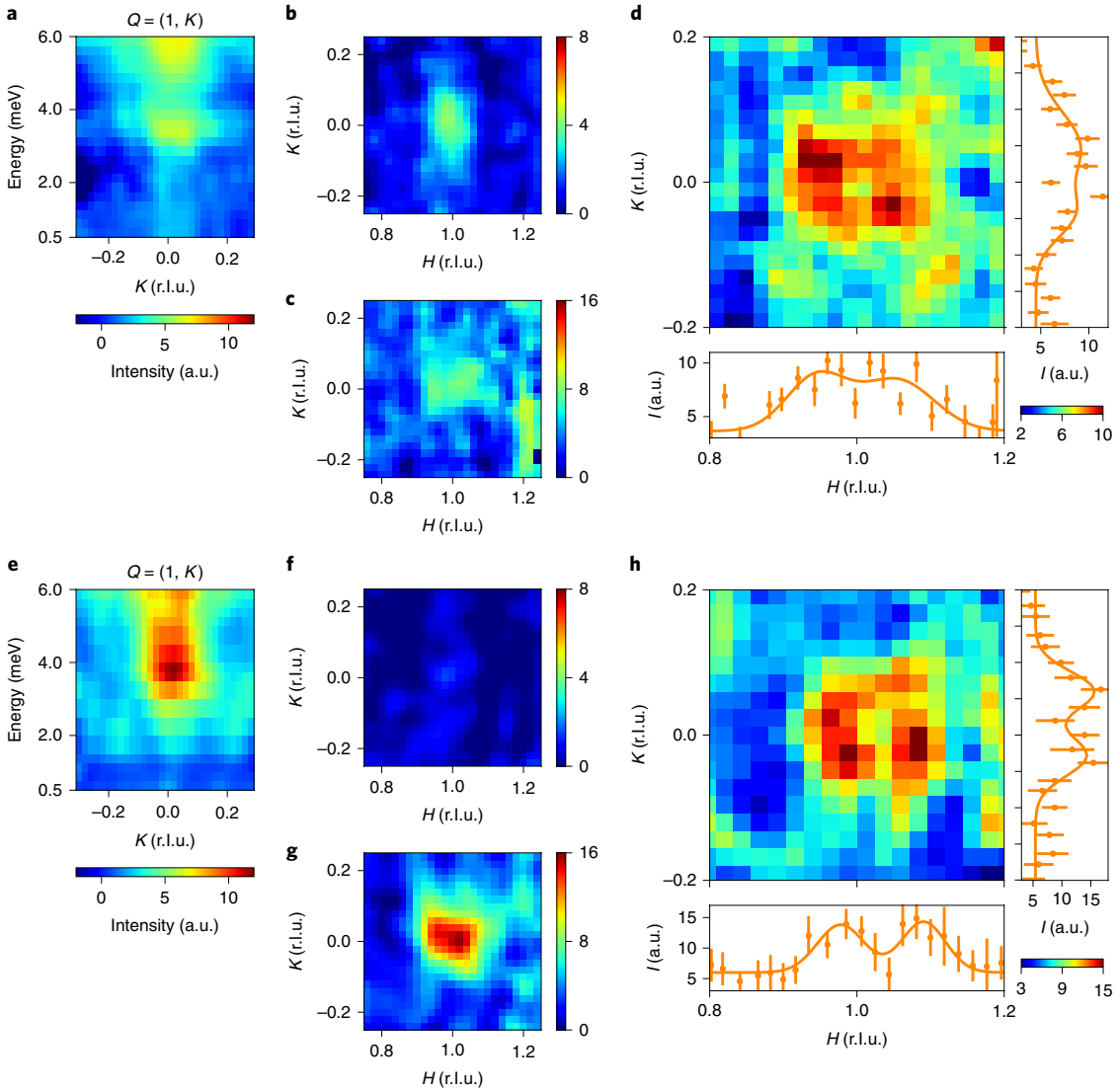

Fig. 2 | Low-energy spin fluctuations in twinned FeSe below and above T_c. a,**e**, Two-dimensional images of a wave-vector and energy dependence of spin fluctuations at $T = 10$ K (**a**) and $T = 2$ K (**e**). **b**–**d**,**f**,**g**, Wave-vector dependence of spin fluctuations in the (H, K) plane at energies $E = 1 \pm 0.25$ meV (**b**,**f**), $E = 3.6 \pm 0.125$ meV (**c**,**g**) and $E = 5.62 \pm 0.125$ meV (**d**). Cuts along the [H, 0] and [1, K] directions with a width of ± 0.04 reciprocal lattice units show a scattering peak with a flattish top near (1, 0). **h**, $E = 5.25 \pm 0.075$ meV. Incommensurate scattering is clearly seen through the identical cuts along the [H, 0] and [1, K] directions. This feature is missed in previous work[18,32,33] due to the small incommensurability and narrow energy range. **a**–**d**, $T = 10$ K; **e**–**h**, $T = 2$ K. Solid lines are fits with the sum of two Gaussians to the data. Colour bars indicate scattering intensity in arbitrary unit (a.u.). The vertical error bars indicate statistical errors of 1 s.d.

coupling in a nematic quantum spin liquid of FeSe can also induce a large superconducting gap and spin excitation anisotropy[19]. To test these hypotheses, we used INS to study the low-energy spin fluctuations in detwinned FeSe (Fig. 1d,e). In the normal state, spin fluctuations from 6 to 11 meV are centred around $\mathbf{Q}_{AF}$ with negligible intensity at (0, ±1), thus exhibiting a pronounced C_2 rotational symmetry as predicted by these theoretical approaches[19,27,31]. By contrast, for energies between 3 and 5 meV the spin fluctuations have a C_4 rotational symmetry magnetic component as shown in the schematic illustration in Fig. 1f,g, which is based on combining experimental evidence from multiple instruments (Supplementary Fig. 10), possibly corresponding to a localized mode in both wave vector and energy. On cooling below T_c, the resonance only appears at $\mathbf{Q}_{AF} = (1, 0)$ (Fig. 1f,g), consistent with the STM observation that superconducting gaps are extremely anisotropic, with minima at the tips of the elliptical pockets. Therefore, while the normal-state C_4 rotational symmetry magnetic component in the 3–5 meV range is not anticipated, the anisotropic superconductivity-induced resonance is consistent with theoretical expectations[19,24].

To detect anisotropic spin fluctuations by INS[32,33], one needs to co-align hundreds of single-crystal FeSe samples. These are grown by the chemical vapour transport method and are about 1–3 mm^2 in size and a few micrometres in thickness (Methods)[9]. Therefore, the most difficult part of carrying out INS experiments on FeSe is to simultaneously detwin hundreds of samples. In previous work on iron pnictides, we were able to completely detwin large (of the order of 0.5–1 cm^2 by a few millimetres in thickness) single crystals of $BaFe_2As_2$ using a mechanical uniaxial pressure device[39,40]. By gluing many oriented FeSe samples on uniaxially pressured $BaFe_2As_2$ as shown schematically in Fig. 1d, we were able to simultaneously detwin many FeSe single crystals required for INS experiments (Supplementary Fig. 2). Figure 1e shows the temperature

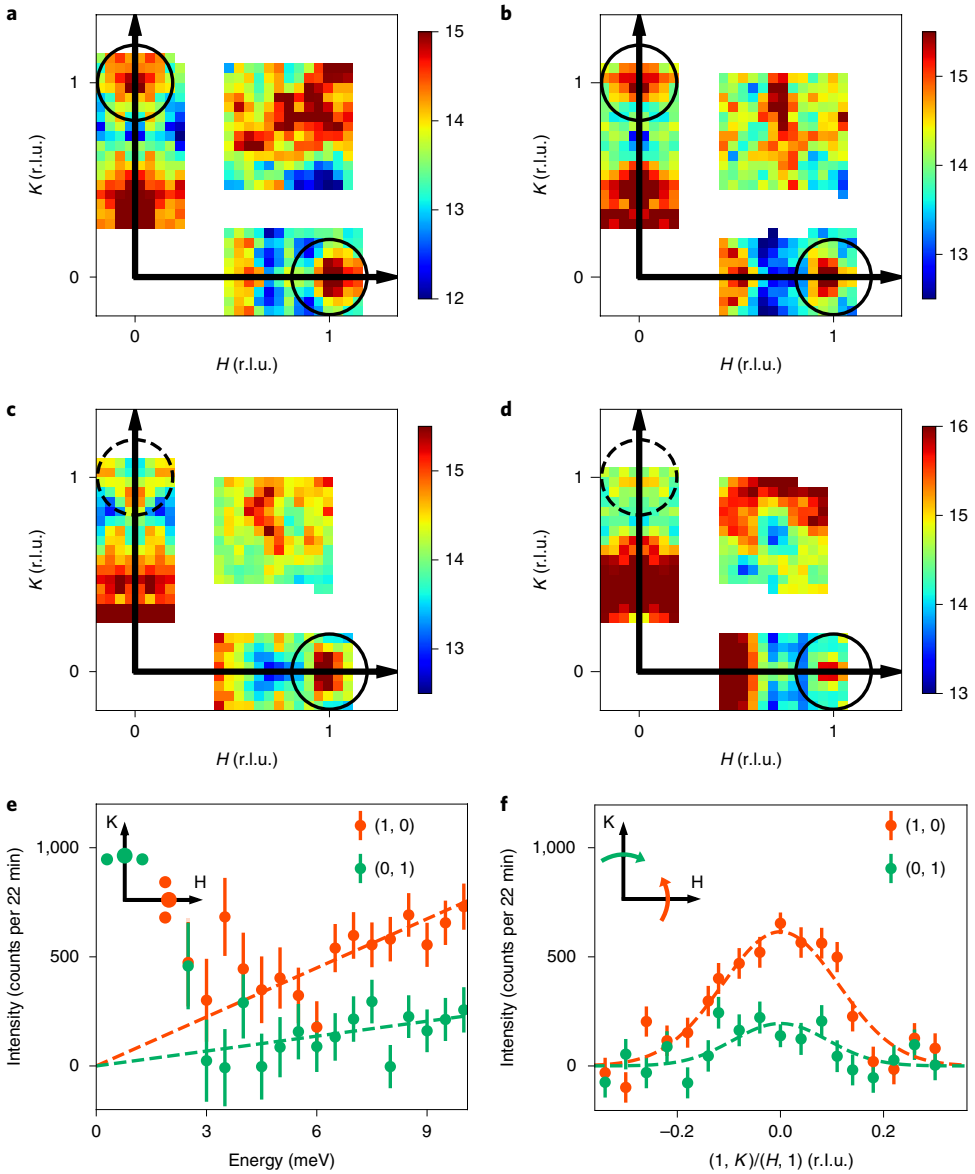

Fig. 3 | Normal-state spin fluctuations in detwinned FeSe. a–d, Two-dimensional images of spin fluctuations at $E=3.5\pm0.5$ meV (**a**), $E=4.5\pm0.5$ meV (**b**), $E=6\pm1$ meV (**c**) and $E=8.5\pm1$ meV (**d**). The data are collected at $T=12$ K using a MAPS chopper spectrometer with incident neutron energy of $E_i=38$ meV along the *c* axis and are folded to improve statistics. The scattering near wave vector (1, 1) is background and not magnetic in origin (Supplementary Figs. 6–8). Colour bars in **a**–**d** indicate scattering intensity in arbitrary units (a.u.). **e**, Energy dependence of the scattering at (1, 0) and (0, 1) above background at $T=11$ K. The positions of signal and background are marked as large and small spots in the inset. **f**, Wave-vector scans at $E=8$ meV along the [1, *K*] (green) and [*H*, 1] directions at $T=11$ K. Linear backgrounds have been subtracted from the data. The vertical error bars indicate the statistical errors of 1 s.d.

dependence of rocking scans along the [*H*, 0, 0] and [0, *K*, 0] directions on multiple FeSe on $BaFe_2As_2$ assemblies. Below $T_s\approx90$ K, we see a clear splitting of the lattice constants. By comparing the scattering intensities of the (2, 0, 0) and (0, 2, 0) nuclear Bragg peaks, we find that the FeSe sample assembly has a detwinning ratio of $\eta=[I(2,0,0)_o-I(0,2,0)_o]/[I(2,0,0)_o+I(0,2,0)_o]\approx50\%$ at 2 K (Fig. 1e), where $I(2,0,0)_o$ and $I(0,2,0)_o$ are the observed Bragg peak intensities at (2, 0, 0) and (0, 2, 0), respectively, below T_s (Supplementary Figs. 3 and 4).

To understand the effect of detwinning FeSe, we first need to determine the wave-vector and energy dependence of the magnetic scattering $S(\mathbf{Q}, E)$ in twinned samples (Methods and Supplementary Fig. 5). Figure 2a,e shows the energy dependence of the magnetic scattering along the [1, *K*] direction above and below T_c, respectively. In the normal state at $T=10$ K, the scattering is gapless above $E=0.5$ meV and exhibits a weak peak around $E=3.2$ meV (Fig. 2a). The spin excitations are centred around $\mathbf{Q}_{AF}=(1,0)$ at $E=1\pm0.25$ meV (Fig. 2b) and 3.625 ± 0.125 meV (Fig. 1c). At $E=5.625\pm0.125$ meV, the spin excitations have a flattish top as revealed by wave-vector cuts along the [*H*, 0] and [1, *K*] directions (Fig. 1d). In the superconducting state at $T=2$ K, a superconductivity-induced spin gap opens below $E\approx2.5$ meV and a resonance forms around $E=3.6$ meV (Figs. 1c and 2e). This is confirmed by the vanishing signal at $E=1\pm0.25$ meV (Fig. 2f) and enhanced magnetic scattering at 3.625 ± 0.125 meV (Fig. 2g). In addition, the resonance is clearly centred at the commensurate $\mathbf{Q}_{AF}=(1,0)$ position (Fig. 2g). However, on increasing the energy to $E=5.25\pm0.075$ meV, we see clear incommensurate ring-like magnetic scattering centred around

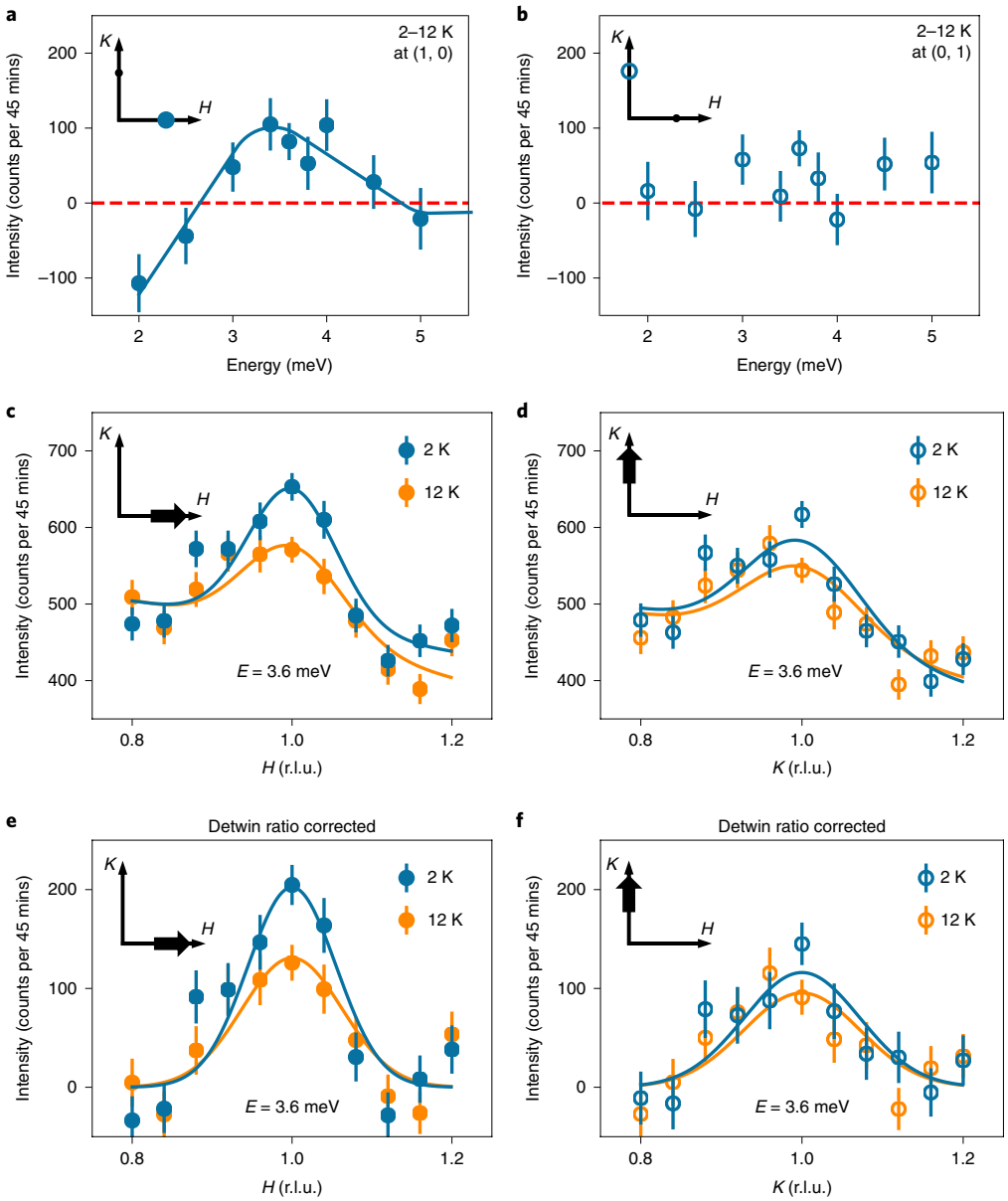

Fig. 4 | Effect of superconductivity on low-energy spin fluctuations of detwinned FeSe. a,**b**, Difference of the scattering in the superconducting state (below T_c) and the normal state plotted as a function of energy for momentum transfers (1, 0) (**a**) and (0, 1) (**b**). The peak seen at $E \approx 3.6$ meV in **a** marks the neutron spin resonance. The solid blue and dashed red lines are guides to the eye. **c**, Wave-vector scans below and above T_c at $E = 3.6$ meV and (1, 0). **d**, Similar scans at (0, 1). **e**,**f**, (1, 0) (**e**) and (0, 1) (**f**) scans with background subtracted and detwinning ratio corrected (Supplementary Fig. 9). The solid lines in **c**–**f** are Gaussian fits to the data before and after linear background subtraction. The vertical error bars indicate the statistical errors of 1 s.d.

$\mathbf{Q}_{AF} = (1, 0)$, as confirmed by wave-vector cuts along the $[H, 0]$ and $[1, K]$ directions (Fig. 2h). The incommensurate scattering intensity in the superconducting state is higher than that in the normal state, suggesting that it is part of the dispersive resonance. In previous work, a dispersive ring-like neutron spin resonance has been seen in the hole-doped $BaFe_2As_2$ family of materials, where the incommensurate scattering has been ascribed to quasiparticle excitations from mismatched hole and electron Fermi surfaces[34].

Figure 3 summarizes the energy evolution of the normal-state spin fluctuations at $\mathbf{Q}_{AF} = (1, 0)$ and (0, 1) in the (H, K) plane in partially detwinned FeSe. Since our FeSe single crystals are mounted on surfaces of $BaFe_2As_2$, one should also see spin fluctuations from $BaFe_2As_2$ at approximately the same position in reciprocal space. However, the spin waves in $BaFe_2As_2$ are gapped below about 10 meV in the low-temperature AF ordered state[41,42], meaning that spin fluctuations at $\mathbf{Q}_{AF} \approx (1, 0)$ and (0, 1) below 10 meV must originate from FeSe. Figure 3a,b shows constant-energy cuts in the (H, K) plane for energy transfers of $E = 3.5 \pm 0.5$ and 4.5 ± 0.5 meV, respectively, in the normal state at $T = 12$ K. We see clear evidence for magnetic scattering at $\mathbf{Q}_{AF} \approx (1, 0)$ and (0, 1) with about the same strength (Supplementary Fig. 6a–d), suggesting a possible mode that has C_4 rotational symmetry in the normal state. On increasing energies to $E = 6 \pm 1$ and 8 ± 1 meV, the scattering at $\mathbf{Q}_{AF} \approx (1, 0)$ becomes much stronger than that at (0, 1), suggesting that spin fluctuations become highly C_2 symmetric at these energies (Fig. 3c,d). To confirm these results, we carried out energy scans at $\mathbf{Q}_{AF} \approx (1, 0)$ and (0, 1) from 2.5 meV to 11 meV as shown in Fig. 3e (Supplementary Fig. 6e). From 6 meV to 11 meV, magnetic scattering at (1, 0) increases in intensity with increasing energy approximately twice as fast as the increase of magnetic scattering at (0, 1). Figure 3f shows wave-vector scans

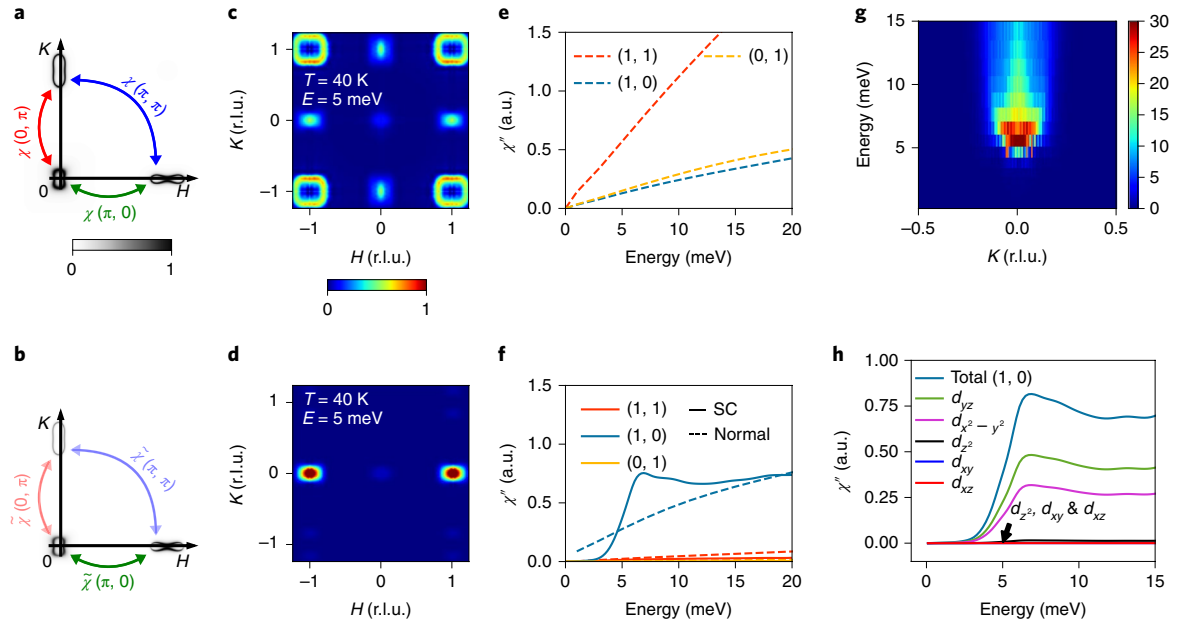

Fig. 5 | Theoretical calculations of the spin fluctuations in detwinned FeSe. a,**b**, Map of the spectral function at zero energy for our model of the electronic structure of FeSe in the fully coherent case with quasiparticle weights $Z_\ell = 1$ (**a**) and the orbital-selective case where reduced quasiparticle weights ($Z_\ell < 1$) (**b**) weaken the spin fluctuations at a certain momentum transfer (blue and red arrows) while the spin fluctuations stemming mostly from the d_{yz} orbital become dominant (green arrow). The grey bar for **a**–**b** represents the intensity of the spectral function. **c**, For the fully coherent model, one obtains in the normal state large contributions to the dynamical structure factor close to (±1, ±1) from the d_{xy} orbital and an almost identical but weaker contribution at (±1, 0) and (0, ±1). The colour code for **c**–**d** shown in the colour bar indicates the calculated intensity maps of the magnetic scattering in arbitrary units (a.u). **e**, The susceptibility integrated around these momentum transfer vectors shows the same trend at low energies. **d**,**f**, In contrast, the orbital-selective model yields spin fluctuations at low energies that are dominated by peaks at (±1, 0) in the low energy range shown. **f**,**g**, The enhancement of the spin fluctuations at (±1, 0) in the superconducting state is clearly seen when plotted as a function of energy (**f**) and as an intensity map in momentum–energy space (**g**). **h**, The spin fluctuations at (1, 0) are dominated by the contributions of the d_{yz} orbital.

approximately along the [1, K] and [H, 1] directions at $E = 8$ meV (see $E = 3.6$ meV data in Supplementary Fig. 6f). The scattering intensity at (1, 0) dominated the signal while spin fluctuations at (0, 1) are only one-third of those at (1, 0). After taking into account the finite η of the FeSe samples (Supplementary Information), there is almost no magnetic scattering at (0, 1) above the background. These results are consistent with Fig. 3c,d, suggesting that the spin fluctuations between 6 and 10 meV are strongly C_2 symmetric.

To confirm that spin fluctuations in FeSe for energies below 5 meV have a C_4 component as suggested in Fig. 3a,b and determine the impact of superconductivity (Supplementary Figs. 7 and 8), we carried out constant-energy and constant-wave-vector scans at (1, 0) and (0, 1) using a cold neutron triple-axis spectrometer (Methods). Figure 4a,b shows temperature difference plots below ($T = 2$ K) and above ($T = 12$ K) T_c as a function of energy at (1, 0) and (0, 1), respectively. In previous work on twinned samples, superconductivity has been found to induce a neutron spin resonance appearing below T_c at (1, 0) and (0, 1) around $E \approx 3.6$ meV (Fig. 1c)[32,33]. While Fig. 4a shows clear evidence for the resonance at $E \approx 3.6$ meV, with intensity reduction (negative scattering) below the mode indicating opening of a spin gap[32,33], an identical temperature difference plot at (0, 1) in Fig. 4b yields no observable temperature difference across T_c, and therefore no superconductivity-induced resonance or spin gap. Figure 4c,d shows wave-vector scans along the [H + 1, 0] and [0, K + 1] directions, respectively, at $E = 3.6$ meV. In the normal state ($T = 12$ K), we see well-defined peaks centred at (1, 0) and (0, 1), consistent with Fig. 3a,b. On cooling below T_c, the scattering at (1, 0) increases in intensity and forms a resonance (Fig. 4c), while it does not change across T_c at (0, 1) (Fig. 4d). Figure 4e,f shows the same data after correcting for background scattering and η. Similarly to Fig. 4c,d, we again find that superconductivity induces a C_2-symmetric resonance on a background of approximately C_4-symmetric normal-state magnetic scattering (Supplementary Fig. 9). Thus, it is the highly anisotropic pairing state of FeSe that drives the C_2-symmetric magnetic scattering at these energies below T_c. Figure 1f,g summarizes the key results of our INS experiments on detwinned FeSe. The deviation of magnetic scattering intensity ratio at (1, 0) and (0, 1) from 3:1 provides convincing evidence for the existence of an unexpected mode. In the normal state, spin fluctuations have approximate C_4 symmetry near the resonance energy but become C_2 symmetric for energies above 6 meV. On entering the superconducting state, a resonance with C_2 symmetry is formed at $\mathbf{Q}_{AF}$ (Fig. 1f and Supplementary Fig. 10).

To achieve a theoretical understanding of the experimental results presented above, we start from an itinerant five-band model that quantitatively matches the low-energy electronic structure of FeSe in its nematic state[9,21,24,36] and compute the magnetic scattering $S(\mathbf{Q}, E) \propto \chi''(\mathbf{Q}, E)/(1 - e^{-E/k_B T})$ where the imaginary part of dynamic susceptibility $\chi''(\mathbf{Q}, E)$ is calculated using a standard random phase approximation formulation[28,29,31,36]. The spectral function at the Fermi level is presented in Fig. 5a. As illustrated in Fig. 5c,e, this 'plain vanilla' approach completely fails, as is evident, for example, from the presence of scattering close to (1, 1), and a negligible (1, 0)–(0, 1) anisotropy. The latter properties can be traced to an improper balance of the three most important scattering channels (Fig. 5a). However, electronic interactions and associated self-energy effects are known to be important in FeSe, constituting an example of a Hund metal[25]. Important properties of Hund's metals include the existence of orbital-dependent mass renormalizations[43–45], and an associated redistribution of the relative importance of different orbital-dependent scattering channels in the spin susceptibility[46].

A simple means to incorporate the important effects of such orbital selectivity is through the introduction of orbital-dependent quasiparticle weights $Z_\ell < 1$ (refs. [31,36]), leading to a modified bare susceptibility $\tilde{\chi}^0_{\ell_1\ell_2\ell_3\ell_4}(\mathbf{Q}, E)$ given by

$$\tilde{\chi}^0_{\ell_1\ell_2\ell_3\ell_4}(\mathbf{Q}, E) = \sqrt{Z_{\ell_1} Z_{\ell_2} Z_{\ell_3} Z_{\ell_4}}\, \chi^0_{\ell_1\ell_2\ell_3\ell_4}(\mathbf{Q}, E). \quad (1)$$

In agreement with theoretical expectations[43–45,47], and earlier detailed studies of tunnelling spectroscopy[24,25], we apply the hierarchy $Z_{xy} < Z_{xz} < Z_{yz}$, which shifts the relative importance of the dominant scattering vectors, as illustrated in Fig. 5b, and thereby modifies the magnetic scattering. As seen in Fig. 5d, the d_{xy}-dominated (1, 1) scattering is strongly reduced (because Z_{xy} is the smallest), and the degree of C_4-symmetry breaking as seen by the difference in the scattering intensities at (±1, 0) versus (0, ±1) is strongly enhanced (because $Z_{xz} < Z_{yz}$), as seen explicitly by the dashed lines in Fig. 5f (Supplementary Fig. 1).

In the superconducting state, we employ a gap structure identical to that of refs. [24,36], which is known to faithfully describe the gap in FeSe, and recalculate the bare susceptibility accordingly[28,36]. When entering the highly anisotropic superconducting state, generated by the orbital-selective spin fluctuations[24,36], a neutron resonance is exhibited solely at the (±1, 0) position as seen from Fig. 5f,g, in agreement with experiments. The associated neutron resonance is highly orbital selective with predominant d_{yz} character, as seen by the orbital-resolved spin susceptibilities plotted in Fig. 5h. Therefore, both the very strong C_4-symmetry breaking in the 5–10 meV range and the unidirectional neutron resonance observed experimentally are captured by the itinerant orbital-selective scenario.

This approach, however, does not provide an explanation for the emergence of the localized approximately C_4-symmetric spin excitations near $E = 3$ meV as shown in Figs. 1f,g and 3a,b. There are several possible scenarios for this remarkable discovery. First, it is possible that self-energy effects in FeSe have a considerably more complicated functional form that cannot be simply captured by including energy- and momentum-independent Z-factors. Second, there is a possibility of impurity-generated low-energy spectral weight similar to the case of cuprates, where vortices and disorder have been shown to generate localized modes in a restricted low-energy regime[48–50]. A counter-argument to the disorder-based scenario, however, is the high quality of the FeSe crystals used in the current experiment (Supplementary Fig. 2).

Finally, if some of the spin excitations in FeSe arise from a local moment quantum paramagnet[16,17,19], the C_2-symmetric AF collinear order competes with the C_4-symmetric Néel order across the nematic ordering temperature T_s (ref. [18]). In this picture, the C_4-symmetric low-energy magnetic excitations with spin-wave ring-like features in detwinned FeSe may simply be the remnant of the localized moment not directly associated with Fermi surface nesting and itinerant electrons.

Regardless of the microscopic origin of the C_4 spin excitations, our data support the notion that the spin fluctuations in the nematic phase of FeSe are, generally, highly anisotropic, and are consistent with superconductivity being driven by spin fluctuations arising mainly from the d_{yz} orbital states. Our measurements highlight the need for a quantitative understanding of the extreme spin anisotropy, as well as the emergence of C_4-symmetric magnetic excitations at the very lowest energies. Progress in this direction may well shed new light on the role of electronic correlations in FeSe in particular, and the origin of unconventional superconductivity in interacting systems in general.

Online content

Any methods, additional references, Nature Research reporting summaries, source data, statements of code and data availability and associated accession codes are available at https://doi.org/10.1038/s41563-019-0369-5.

Received: 4 September 2018; Accepted: 10 April 2019;
Published online: 20 May 2019

References

1. Scalapino, D. J. A common thread: the pairing interaction for unconventional superconductors. *Rev. Mod. Phys.* **84**, 1383 (2012).
2. Dai, P. C. Antiferromagnetic order and spin dynamics in iron-based superconductors. *Rev. Mod. Phys.* **87**, 855 (2015).
3. Chu, J.-H. et al. In-plane resistivity anisotropy in an underdoped iron arsenide superconductor. *Science* **329**, 824–826 (2010).
4. Kuo, H.-H., Chu, J.-H., Palmstrom, J. C., Kivelson, S. A. & Fisher, I. R. Ubiquitous signatures of nematic quantum criticality in optimally doped Fe-based superconductors. *Science* **352**, 958–962 (2016).
5. Fernandes, R. M., Chubukov, A. V. & Schmalian, J. What drives nematic order in iron-based superconductors? *Nat. Phys.* **10**, 97–104 (2014).
6. Böhmer, A. E. & Meingast, C. Electronic nematic susceptibility of iron-based superconductors. *C. R. Phys.* **17**, 90–112 (2016).
7. Hsu, F. C. et al. Superconductivity in the PbO-type structure α-FeSe. *Proc. Natl Acad. Sci. USA* **105**, 14262 (2008).
8. McQueen, T. M. et al. Tetragonal-to-orthorhombic structural phase transition at 90 K in the superconductor $Fe_{1.01}Se$. *Phys. Rev. Lett.* **103**, 057002 (2009).
9. Böhmer, A. E. & Kreisel, A. Nematicity, magnetism and superconductivity in FeSe. *J. Phys.: Condens. Matter* **30**, 023001 (2018).
10. Lee, C. C., Yin, W.-G. & Ku, W. Ferro-orbital order and strong magnetic anisotropy in the parent compounds of iron-pnictide superconductors. *Phys. Rev. Lett.* **103**, 267001 (2009).
11. Baek, S.-H. et al. Orbital-driven nematicity in FeSe. *Nat. Mater.* **14**, 210–214 (2015).
12. Böhmer, A. E. et al. Origin of the tetragonal-to-orthorhombic phase transition in FeSe: a combined thermodynamic and NMR study of nematicity. *Phys. Rev. Lett.* **114**, 027001 (2015).
13. Yamakawa, Y., Onari, S. & Kontani, H. Nematicity and magnetism in FeSe and other families of Fe-based superconductors. *Phys. Rev. X* **6**, 021032 (2016).
14. Onari, S., Yamakawa, Y. & Kontani, H. Sign-reversing orbital polarization in the nematic phase of FeSe due to the C_2 symmetry breaking in the self-energy. *Phys. Rev. Lett.* **116**, 227001 (2016).
15. Kontani, H. & Onari, S. Orbital-fluctuation-mediated superconductivity in iron pnictides: analysis of the five-orbital Hubbard-Holstein model. *Phys. Rev. Lett.* **104**, 157001 (2010).
16. Wang, F., Kivelson, S. & Lee, D.-H. Nematicity and quantum paramagnetism in FeSe. *Nat. Phys.* **11**, 959–963 (2015).
17. Glasbrenner, J. K. et al. Effect of magnetic frustration on nematicity and superconductivity in iron chalcogenides. *Nat. Phys.* **11**, 953–958 (2015).
18. Wang, Q. et al. Magnetic ground state of FeSe. *Nat. Commun.* **7**, 12182 (2016).
19. She, J.-H., Lawler, M. J. & Kim, E.-A. Quantum spin liquid intertwining nematic and superconducting order in FeSe. *Phys. Rev. Lett.* **121**, 237002 (2018).
20. Yi, M., Zhang, Y., Shen, Z.-X. & Lu, D. Role of the orbital degree of freedom in iron-based superconductors. *npj Quantum Mater.* **2**, 57 (2017).
21. Coldea, A. & Watson, M. D. The key ingredients of the electronic structure of FeSe. *Annu. Rev. Condens. Matter Phys.* **9**, 125–146 (2018).
22. Liu, D. F. et al. Orbital origin of extremely anisotropic superconducting gap in nematic phase of FeSe superconductor. *Phys. Rev. X* **8**, 031033 (2018).
23. Song, C. L. et al. Imaging the electron boson coupling in superconducting FeSe films using a scanning tunneling microscope. *Phys. Rev. Lett.* **112**, 057002 (2014).
24. Sprau, P. O. et al. Discovery of orbital-selective Cooper pairing in FeSe. *Science* **357**, 75–80 (2017).
25. Kostin, A. et al. Visualizing orbital-selective quasiparticle interference in the Hund's metal state of FeSe. *Nat. Mater.* **17**, 869–874 (2018).
26. Wang, Z. T., Hu, W. J. & Nevidomskyy, A. H. Spin ferroquadrupolar order in the nematic phase of FeSe. *Phys. Rev. Lett.* **116**, 247203 (2016).
27. Lai, H.-H., Hu, W. J., Nica, E. M., Yu, R. & Si, Q. Antiferroquadrupolar order and rotational symmetry breaking in a generalized bilinear-biquadratic model on a square lattice. *Phys. Rev. Lett.* **118**, 176401 (2017).
28. Kreisel, A., Mukherjee, S., Hirschfeld, P. J. & Andersen, B. M. Spin excitations in a model of FeSe with orbital ordering. *Phys. Rev. B* **92**, 224515 (2015).
29. Mukherjee, S., Kreisel, A., Hirschfeld, P. J. & Andersen, B. M. Model of electronic structure and superconductivity in orbitally ordered FeSe. *Phys. Rev. Lett.* **115**, 026402 (2015).
30. Hirschfeld, P. J. Using gap symmetry and structure to reveal the pairing mechanism in Fe-based superconductors. *C. R. Phys.* **17**, 197–231 (2016).
31. Kreisel, A., Andersen, B. M. & Hirschfeld, P. J. Itinerant approach to magnetic neutron scattering of FeSe: effect of orbital selectivity. *Phys. Rev. B* **98**, 214518 (2018).

32. Wang, Q. et al. Strong interplay between stripe spin fluctuations, nematicity and superconductivity in FeSe. *Nat. Mater.* **15**, 159–163 (2016).
33. Ma, M. W. et al. Prominent role of spin-orbit coupling in FeSe revealed by inelastic neutron scattering. *Phys. Rev. X* **7**, 021025 (2017).
34. Zhang, R. et al. Neutron spin resonance as a probe of Fermi surface nesting and superconducting gap symmetry in $Ba_{0.67}K_{0.33}(Fe_{1-x}Co_x)_2As_2$. *Phys. Rev. B* **98**, 060502(R) (2018).
35. Nica, E. M., Yu, R. & Si, Q. Orbital-selective pairing and superconductivity in iron selenides. *npj Quantum Mater.* **2**, 24 (2017).
36. Kreisel, A. et al. Orbital selective pairing and gap structures of iron-based superconductors. *Phys. Rev. B* **95**, 174504 (2017).
37. Benfatto, L., Valenzuela, B. & Fanfarillo, L. Nematic pairing from orbital selective spin fluctuations in FeSe. *npj Quantum Mater.* **3**, 56 (2018).
38. Kang, J., Fernandes, R. M. & Chubukov, A. Superconductivity in FeSe: the role of nematic order. *Phys. Rev. Lett.* **120**, 267001 (2018).
39. Lu, X. Y. et al. Nematic spin correlations in the tetragonal state of uniaxial-strained $BaFe_{2-x}Ni_xAs_2$. *Science* **345**, 657 (2014).
40. Lu, X. Y. et al. Spin waves in detwinned $BaFe_2As_2$. *Phys. Rev. Lett.* **121**, 067002 (2018).
41. Matan, K., Morinaga, R., Iida, K. & Sato, T. J. Anisotropic itinerant magnetism and spin fluctuations in $BaFe_2As_2$: a neutron scattering study. *Phys. Rev. B* **79**, 054526 (2009).
42. Wang, C. et al. Longitudinal spin excitations and magnetic anisotropy in antiferromagnetically ordered $BaFe_2As_2$. *Phys. Rev. X* **3**, 041036 (2013).
43. Georges, A., de' Medici, L. & Mravlje, J. Strong correlations from Hund's coupling. *Annu. Rev. Condens. Matter Phys.* **4**, 137–178 (2013).
44. de' Medici, L. & Capone, M. in *The Iron Pnictide Superconductors* (eds Mancini, F. & Citro, R.) 186 (Springer, 2017).
45. van Roekeghem, A., Richard, P., Ding, H. & Biermann, S. Spectral properties of transition metal pnictides and chalcogenides: angle-resolved photoemission spectroscopy and dynamical mean-field theory. *C. R. Phys.* **17**, 140 (2016).
46. Ishizuka, J., Yamada, T., Yanagi, Y. & Ono, Y. Fermi surface, pressure-induced antiferromagnetic order, and superconductivity in FeSe. *J. Phys. Soc. Jpn* **87**, 014705 (2018).
47. Yu, R., Zhu, J.-X. & Si, Q. Orbital selectivity enhanced by nematic order in FeSe. *Phys. Rev. Lett.* **121**, 227003 (2018).
48. Lake, B. et al. Spins in the vortices of a high-temperature superconductor. *Science* **291**, 1759 (2001).
49. Kimura, H. et al. Novel in-gap spin state in Zn-doped $La_{1.85}Sr_{0.15}CuO_4$. *Phys. Rev. Lett.* **91**, 067002 (2003).
50. Andersen, B. M. et al. Disorder-induced freezing of dynamical spin fluctuations in cuprate materials. *Phys. Rev. Lett.* **105**, 147002 (2010).

Acknowledgements

We thank D. Abernathy, Q. Wang, Y. Hao and H. Hu for useful discussions. The neutron-scattering work at Rice University was supported by the US Department of Energy, BES DE-SC0012311 (P.D.). The single-crystal synthesis work was supported by Robert A. Welch Foundation grant no. C-1839 (P.D.). X.L. is supported by the National Natural Science Foundation of China under Grant No. 11734002. C.B. and Y.C. are supported by the US Department of Energy grant no. DE-FG02-08ER46544. B.M.A. acknowledges financial support from the Carlsberg Foundation. P.J.H. was supported by the Department of Energy under grant no. DE-FG02-05ER46236. This research used resources at the High Flux Isotope Reactor and Spallation Neutron Source, a DOE Office of Science User Facility operated by the Oak Ridge National Laboratory. Access to MACS was provided by the Center for High Resolution Neutron Scattering, a partnership between the National Institute of Standards and Technology and the National Science Foundation under agreement No. DMR-1508249.

Author contributions

X.L., T.C. and P.D. conceived the project. T.C. prepared all the FeSe single-crystal samples. $BaFe_2As_2$ single crystals were prepared by T.C., X.L., R.Z., Y.L. and Y.R. Neutron-scattering experiments on twinned samples were carried out by T.C., Y.C., Y.Q., C.B. and P.D. at NCNR. Neutron-scattering experiments on detwinned samples were carried out by T.C., J.P., T.G.P., J.R.S., H.C., Y.W. and P.D. at Oak Ridge National Laboratory, ISIS and MLZ. Theoretical analysis was performed by A.K., B.M.A. and P.J.H. The entire project was supervised by P.D. The manuscript was written by P.D., T.C., A.K., B.M.A. and P.J.H. All authors made comments.

Competing interests

The authors declare no competing interests.

Additional information

Supplementary information is available for this paper at https://doi.org/10.1038/s41563-019-0369-5.

Reprints and permissions information is available at www.nature.com/reprints.

Correspondence and requests for materials should be addressed to X.L. or P.D.

Publisher's note: Springer Nature remains neutral with regard to jurisdictional claims in published maps and institutional affiliations.

Methods

Experimental setups. Elastic neutron experiments were carried out on the HB-3A four-circle diffractometer at the High Flux Isotope Reactor, Oak Ridge National Laboratory, United States, to first check if the method works well in detwinning FeSe on a single piece of $BaFe_2As_2$ (Supplementary Fig. 3). HB-3A uses a silicon monochromator and a scintillator-based two-dimensional $(H, K, L) = (q_x a_o/2\pi, q_y b_o/2\pi, q_z c/2\pi)$ in reciprocal lattice units using the orthorhombic lattice notation for FeSe, where $a_o \approx 5.33$ Å, $b_o \approx 5.31$ Å, $c = 5.486$ Å (ref. [9]).

Our INS experiments on twinned samples were done on the MACS cold triple-axis spectrometer at NIST Center for Neutron Research at Gaithersburg, MD. The MACS spectrometer has a double focusing pyrolytic graphite (PG(002)) monochromator and multiple detectors. We used fixed scattered neutron energy $E_f = 3.7$ meV with a BeO filter after the sample and a Be filter before the monochromator for energy transfers below $E = 1.5$ meV.

Our INS experiments on detwinned samples were carried out on the PANDA cold neutron and PUMA thermal neutron triple-axis spectrometers at MLZ, Garching, Germany[39], and on the MAPS time-of-flight chopper spectrometer at ISIS, Rutherford-Appleton laboratory, Didcot, United Kingdom[40].

For PANDA experiments, a double-focused pyrolytic graphite (PG(002)) monochromator and analyser with $E_f = 5.1$ meV were used with collimations of none–40′–40′–none for inelastic measurements. For elastic measurements, we used $E_f = 4.39$ meV with collimations of 80′–80′–80′–80′. For thermal neutron measurements on PUMA, we used $E_f = 14.69$ meV with double focusing monochromator and analyser and no collimators. For MAPS neutron time-of-flight measurements, we used an incident beam energy of $E_i = 38$ meV with the incident beam along the c axis of the crystal.

Sample growth and preparation. The high-quality FeSe single crystals used in the experiments were grown by a chemical vapour transport method. Fe and Se powder were sealed in quartz tubes with $KCl–AlCl_3$ flux. The growth took 28 d in a temperature gradient from 330 °C to 400 °C. Typical samples are 1×1 mm^2 in area and less than 0.1 mm in thickness. The square $BaFe_2As_2$ crystals were grown using a flux method[40]. They were aligned using a Laue camera and cut along the tetragonal [1, 1, 0] and [1, −1, 0] directions with a high-precision wire saw. Since single crystals of FeSe have one natural edge 45° rotated from the orthorhombic a_o direction, we can use an optical method to co-align FeSe on the surface of $BaFe_2As_2$. Given our intent to measure spin excitations in detwinned FeSe, we aligned and glued (with CYTOP type M) about 300 small pieces of FeSe single crystals on many pieces of large $BaFe_2As_2$ single crystals (Supplementary Figs. 1 and 3).

Data availability

The data that support the plots in this paper and other findings of this study are available from the corresponding authors on reasonable request.